Pi International Journal of Mathematical Sciences
Volume 2 | Issue 2 | April 2026 | ISSN: 3107-9830 (Online)
Available online at: https://pijms.com/
DOI: https://doi.org/10.59828/pijms.v2i2.30

Transient Elastico-Viscous Boundary Layer Thermal Transport with Stagnation-Point Slip Flow Over a Stretching Surface

Bikash Koli Saha

Independent Researcher, Mathematics, City: Guwahati, State: Assam, Pin Code: 781018, Country: India
Email: *bikashkoli100@gmail.com*

Received: 09 March 2026 | **Accepted:** 07 April 2026 | **Published:** 29 April 2026

Abstract

The unsteady boundary-layer dynamics governing momentum and thermal transport induced by a stretching surface within an elastico-viscous medium are systematically examined. The surface interaction is modelled through a non-standard partial slip formulation, facilitating a refined characterization of near-wall kinematics. The constitutive behaviour of the elastico-viscous fluid is represented via Walters' liquid Model B′, thereby accounting for memory-dependent rheological effects. Through the imposition of judiciously selected similarity transformations, the fundamental conservation equations are transmuted into a dimensionally contracted, self-similar construct, thereby rendering the system tractable for subsequent numerical interrogation. Computational resolution of the resulting boundary-value problem is executed through MATLAB's inbuilt collocation algorithm ***bvp4c****, yielding velocity and thermal fields as well as ancillary transport parameters. Parametric interrogation highlights the pronounced influence of unsteadiness, surface slip, and elastico-viscosity on the emergent flow architecture. Results elucidate that the elastico-viscous modulus, velocity ratio, and both kinematic and thermal slip coefficients exert dominant control over momentum transport and heat transfer characteristics under slip and no-slip configurations. The investigation further establishes that the velocity and thermal distributions exhibit acute sensitivity to variations in the embedded flow-control parameters.*

Keywords: *Elastico-viscous fluid; Walters' liquid Model B′; Unsteady boundary-layer flow; Partial slip; Heat transfer.*
Mathematics Subject Classification (MSC) 2020: *76A05, 76D10, 80A20.*

1. Introduction

The practical impetus of the present investigation emerges from the coupled momentum and energy transport phenomena engendered by stretching surface flows, which constitute canonical configurations in numerous industrial and technological operations. The thermal regulation within such processes exerts a decisive role in dictating product quality, with the cooling rate functioning as a critical determinant of microstructural and performance characteristics. Accordingly, precise modulation of heat transfer is indispensable for the realization of superior end products. From a theoretical standpoint, the boundary-layer construct assumes paramount importance in fluid mechanics, insofar as the entire dynamical evolution of the flow field is orchestrated by surface-imposed kinematic constraints. Boundary-layer theory thus provides the foundational paradigm for characterizing diverse classes of fluids, wherein similarity transformations facilitate the reduction of governing conservation laws into analytically and computationally tractable self-similar formulations.

A substantial class of technologically indispensable working fluids manifest non-Newtonian rheological behaviour, whose prevalence has rendered them more realistic and industrially germane than their Newtonian counterparts. Such viscoelastic media simultaneously embody dissipative (viscous) and restorative (elastic) attributes, thereby exhibiting dualistic mechanical responses. Under high-rate compressive or shear loading, these complex fluids undergo rheo-thickening transitions,

wherein structural rearrangements promote an apparent solidification, a property extensively harnessed in the design of impact-mitigating and protective systems. The archetypal paradigm of non-Newtonian transport induced by stretching-sheet kinematics has therefore emerged as a canonical model with direct translational relevance to numerous processing technologies. Notable exemplars include fibre spinning, extrusion of polymeric and plastic films, papermaking operations, hot rolling of metals, continuous casting, wire coating, and thermomechanical treatments in food engineering.

When a rigid obstruction intercepts the incoming stream such that the local velocity field asymptotically vanishes, a hydrodynamic stagnation regime is established. This canonical flow configuration arises in diverse engineering and biomedical contexts, notably in aerodynamic filtration technologies and in dental fluidic applications, where stagnation-point dynamics govern operational efficiency. The coupled variations in thermal and momentum transport characteristics of viscous media in the immediate neighbourhood of such stagnation zones have been rigorously analysed by Mahapatra et al. *(*2002), specifically within the framework of the hydrodynamic evolution of the viscous boundary-layer engendered by the kinematic actuation of a surface undergoing monotonic linear extensional deformation. Nazar et al. (2004) conducted a detailed examination of temporally evolving stagnation-point flow impinging upon a continuously deforming surface, thereby elucidating the unsteady hydrodynamic adjustments in the near-wall regime. Hayat et al. (2009) extended the paradigm by incorporating magneto hydrodynamic (MHD) effects into the analysis of micro polar fluid transport induced by nonlinear stretching kinematics, capturing the intricate interplay between spin inertia, microstructural rotations, and electromagnetic body forces. Complementarily, Mukhopadhyay and Swati (2010) delineated the thermal transport characteristics associated with mixed convection instabilities, demonstrating the coupled free- and forced-convective heat transfer mechanisms along a vertically stretching surface undergoing unsteady expansion.

In numerous dynamical configurations wherein the governing flow is explicitly time-dependent, hydrodynamic instabilities are recurrently manifested. Ishak et al. (2008) provided a systematic characterization of the boundary-layer development of an initially quiescent medium driven by a stretching surface. Bhattacharyya et al. (2011) advanced this framework by incorporating partial slip effects within the near-wall stagnation-point regime contiguous to a surface subjected to unidirectional contractive kinematic deformation, thereby highlighting the modified near-wall kinematics. In a subsequent contribution, Bhattacharyya (2013) analysed the coupled heat transfer processes associated with contracting and expanding sheets, with particular emphasis on Casson fluid rheology in the stagnation-point vicinity. Complementary investigations into the momentum–thermal transport mechanisms proximal to stagnation regions were carried out by Khalid et al. (2016), Seth et al. (2017), Dzulkifli et al. (2018), and Rosali et al. (2020), each considering distinct parametric influences and fluid-dynamical attributes.

Layek et al. (2018) initiated the analytical exploration of convective thermal transport characteristics coupled with hydrodynamic symmetry phenomena within the theologically complex framework of non-Newtonian media by considering a power-law fluid subjected to thermal radiation effects over a nonlinearly contracting/expanding sheet. Mabood et al. (2019) pursued a numerical investigation into the role of velocity slip on coupled momentum, mass, and energy transport within magneto hydrodynamic (MHD) unsteady stretching-surface flows. Alghamdi et al. (2021) examined hybrid nanofluid transport phenomena in the stagnation-point vicinity of a stretched surface, thereby elucidating nanoparticle–base fluid interactions under near-wall acceleration. Incorporating slip effects, Agrawal et al. (2021) analysed magneto-hydrodynamic transport dynamics and associated thermos-physical responses engendered within a nonlinear deformation-ally extensible porous medium sheet, emphasizing modified permeability–electromagnetic interactions. Mabood et al. (2022) demonstrated the viscoelastic rheology of nanofluid transport along a stretching cylindrical geometry, capturing curvature-induced modifications. A series of investigations by Debnath and Saha (2020); Debnath and Saha (2022) systematically addressed the elastico-viscous fluid dynamics under varying geometric constraints, while Saha and Debnath (2023) further extended this framework to encompass the spatiotemporal dispersion dynamics of a chemically reactive solutal species permeating an elastico-viscous continuum in the vicinity of a flat, fluid-permeable plate.

Raza and Ashfaq (2025) conducted a thermo-hydrodynamic optimization of biphasic nanofluid transport across a biaxially extensible substrate through the deployment of an integrated Taguchi–Grey Relational Analysis (GRA) scheme. Advancing

this optimization paradigm, Raza and Mustafa et al. (2024) operationalized Response Surface Methodology (RSM) to amplify the thermal transport rate of trihybrid nanofluidic suspensions constrained between coaxial horizontal cylinders. Concurrently, Raza, et al. (2024) adopted a Fuzzy TOPSIS-based multi-attribute decision-making protocol to refine the magneto-hydrodynamic (MHD) efficacy of trihybrid nanofluids in heat-pipe configurations. In a related extension, Shutaywi et al. (2024) scrutinized the optimization of magnetized tetra-hybrid nanofluid dynamics within a channel delimited by deformation-ally extensible boundaries, whereas Shutaywi et al. (2025) elucidated the mechanisms of thermal augmentation in trihybrid Casson nanofluid flow past a quadratic-ally stretching sheet, underscoring the superior thermos-physical leverage of hybrid-suspension architectures in advanced optimization frameworks.

This work examines the motion of fluids and the transfer of heat across a stretching surface in an unstable elastico-viscous boundary layer using Walters Liquid (Model B′).

2. Formulation of the Problem

The thermal transport phenomena associated with the transient hydrodynamic evolution of boundary-layer structures within an elastico-viscous continuum localized in the near-field domain of a stagnation-point configuration are investigated for a continuously deforming surface characterized by the stretching velocity $U_w(x,t)$. The wall temperature distribution, denoted as $T_w\ (x,t)$, is assumed to exhibit spatio-temporal variability along the axial coordinate of the sheet. The governing hydrodynamic and energy transport mechanisms are encapsulated within the subsequent system of differential equations (2011):

$$u_x + v_y = 0 \tag{2.1}$$

$$u_t + uu_x + vu_y = -\frac{1}{\rho}p_x + \nu u_{yy} \; -$$

$$k_0(\rho)^{-1}\left(u_{tyy} + uu_{xyy} + vu_{yyy} - u_y u_{xy} - v_y u_{yy}\right) \tag{2.2}$$

$$T_t + uT_x + vT_y = K\left(\rho C_p\right)^{-1} T_{yy} \tag{2.3}$$

where u represents the velocity component aligned with the stream-wise x direction, v represents the velocity vector projection resolved in the direction of the corresponding coordinate axis, transverse y direction, while the remaining notations preserve their conventional definitions in accordance with the established continuum mechanics framework.

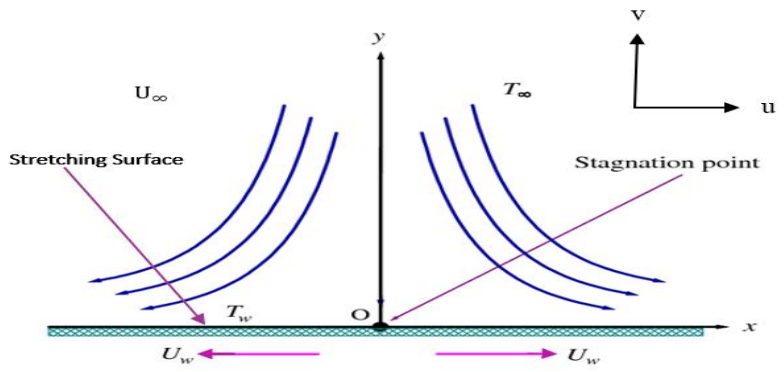

Figure. 2.1. Schematic Representation of the Physical Configuration of the Flow

In the asymptotic region corresponding to the free-stream, wherein viscous effects are negligible, the stream-wise velocity component satisfies $u = U_\infty(x,t)$. Consequently, invoking relation (2.2), one may reformulate the governing expression as follows:

$$(U_\infty)_t + U_\infty(U_\infty)_x = -(\rho)^{-1}p_x \tag{2.4}$$

where U_∞ designates the characteristic stagnation-point velocity of the external inviscid free-stream.

Accordingly, expression (2.2) can be recast in the following form:

$$u_t + uu_x + vu_y = (U_\infty)_t + U_\infty(U_\infty)_x + \nu u_{yy} \; -$$

$$\frac{k_0}{\rho}\left(u_{tyy} + uu_{xyy} + vu_{yyy} - u_y u_{xy} - v_y u_{yy}\right) \tag{2.5}$$

The corresponding set of physically admissible boundary constraints may be expressed as follows:

$$u = U_w(x,t) + N_1 \upsilon u_y, v = 0 \text{ at } y = 0;$$

$$u \to U_\infty(x,t) \text{ as } y \to \infty \qquad (2.6)$$

$$T = T_w + D_1 T_y \text{ at } y = 0;\ T \to T_\infty \text{ as } y \to \infty \qquad (2.7)$$

The admissible analytical representations for the stretching velocity and the external stagnation-point flow are prescribed as $U_w(x,t) = cx(1-\alpha t)^{-1}$ and $U_\infty(x,t) = ax(1-\alpha t)^{-1}$, respectively, where $c(>0)$: denotes the stretching-rate parameter, $\alpha(>0)$ is a temporal modulation constant, and $a(>0)$: characterizes the straining intensity of the ambient stream. The kinematic and thermal slip mechanisms at the surface are incorporated through the velocity slip coefficient $N_1(=N\sqrt{1-\alpha t})$: and the thermal slip coefficient $D_1(=D\sqrt{1-\alpha t})$: , wherein $N$and D correspond to the initial (time-independent) velocity and thermal slip coefficients, respectively.

The functional specification for the wall temperature distribution $T_w\ (x,t)$ is prescribed in the form of Bhattacharyya et al. (2011):

$$T_w = T_\infty + T_0(cx^2)(2\upsilon)^{-1}(1-\alpha t)^{-\frac{3}{2}} \qquad (2.8)$$

where T_∞ characterizes the asymptotically uniform ambient free-stream thermal state, while T_0 constitutes an invariant control parameter modulating the gradient of spatiothermal variation imposed along the surface boundary.

The transformation of the governing system is facilitated through the introduction of the following similarity variables by Bhattacharyya et al. (2011):

$$\psi = \left(\frac{c\upsilon}{1-\alpha t}\right)^{\frac{1}{2}} x f(\eta),\ T = T_\infty + (T_w - T_\infty)\theta(\eta), \text{and } \eta = y\left(\frac{c}{\upsilon(1-\alpha t)}\right)^{\frac{1}{2}} \qquad (2.9)$$

subject to the kinematic relations $u = \psi_y$ and $v = -\psi_x$, wherein ψ denotes the stream function ensuring automatic satisfaction of the continuity constraint, and η represents the similarity variable introduced for similarity reduction:

In light of the similarity transformation (2.9), the governing relations (2.5) and (2.3) are reformulated into the following reduced forms:

$$f'''(\eta) + f(\eta)f''(\eta) - \{f'(\eta)\}^2 - A\{f'(\eta) + \frac{\eta}{2}f''(\eta) - \frac{a}{c}\} + \left(\frac{a}{c}\right)^2 - k_1\left[A\frac{\eta}{2}f^{iv}(\eta) + 2Af'''(\eta) - f(\eta)f^{iv}(\eta) + 2f'(\eta)f'''(\eta) - \{f''(\eta)\}^2\right] = 0 \qquad (2.10)$$

$$\theta''(\eta) + \Pr\left[\begin{matrix} f(\eta)\theta'(\eta) - 2f'(\eta)\theta(\eta) - \\ \frac{A}{2}\{3\theta(\eta) + \eta\theta'(\eta)\} \end{matrix}\right] = 0 \qquad (2.11)$$

where the non-dimensional ratio $\frac{a}{c}$ embodies the velocity control parameter, $A = \frac{\alpha}{c}$ prescribes the unsteadiness index governing temporal flow modulation, and $Pr = \frac{\mu c_p}{k}$ represents the Prandtl number, a canonical dimensionless group delineating the relative dominance of momentum diffusivity over thermal diffusivity in the transport regime.

The boundary constraints, upon application of the similarity transformations, reduce to the following canonical form:

$$f(\eta) = 0,\ f'(\eta) = 1 + \lambda f''(\eta), \theta(\eta) = 1 + \delta\theta'(\eta)\ at\ \eta = 0 \qquad (2.12)$$

$$f'(\eta) = \frac{a}{c},\ f''(\eta) = 0, \theta(\eta) \to 0\ as\ \eta \to \infty \qquad (2.13)$$

where $\lambda = N\sqrt{c\upsilon}$: transformed velocity slip parameter and $\delta = D\sqrt{\frac{c}{\upsilon}}$: transformed thermal slip parameter.

3. SOLUTION SCHEME

For implementation within the MATLAB inbuilt well-posed boundary-conditioned operator solver **bvp4c**, equations (2.10) and (2.11) are recast into the following reduced system

$$f = y_1, f' = y_2,\ f'' = y_3, f''' = y_4\ , \theta = y_5, \theta' = y_6 \qquad (3.1)$$

On the basis of relation (3.1), the governing expression can be reformulated as:

$$y_1' = y_2, y_2' = y_3, y_3' = y_4, y_5' = y_6 \qquad (3.2)$$

By employing the transformations (3.1) and (3.2), the governing relations (2.10) and (2.11) are reformulated into the following equivalent forms:

$$y_4^{/} = \frac{1}{\left(A\frac{\eta}{2} - y_1\right)}[y_3^2 - 2y_2y_4 - 2Ay_4 - \frac{1}{k_1}\left\{y_4 + y_1y_3 - y_2^2 - A\left(y_2 + \frac{\eta}{2}y_3 - \frac{a}{c}\right) + \left(\frac{a}{c}\right)^2\right\}] \qquad (3.3)$$

$$y_6^{/} = -\Pr\left\{y_1y_6 - 2y_2y_5 - \frac{A}{2}(3y_5 + \eta y_6)\right\} \qquad (3.4)$$

Correspondingly, the boundary constraints specified in (2.12) and (2.13) reduce to the following form:

$$y_1(0) = 0, y_2(0) = 1+\lambda y_3(0)\ and\ \ y_5(0) = 1 + \delta y_6(0) \qquad (3.5)$$

$$y_2(\infty) = \frac{a}{c}, y_3(\infty) = 0 \quad and\ \ y_5(\infty) \qquad (3.6)$$

The foregoing reduced equations constitute the computational framework for the numerical implementation, wherein the pertinent flow-governing parameters are invoked to generate the spatial distributions of the velocity and thermal fields.

4. RESULTS AND DISCUSSION

The numerical simulations are executed through MATLAB's built-in collocation-based boundary-value solver **bvp4c**, wherein velocity and thermal field profiles are generated to elucidate the influence of pertinent flow parameters and to highlight their physical implications on the overall flow structure. Graphical interpretations corresponding to these parametric effects are provided in Figs. 4.1–4.12. For validation purposes, the numerically obtained numerical magnitudes of the dimensionless wall-shear indicator $f''(0)$, computed via the implemented solver, are benchmarked against established results available in the open literature. The present findings exhibit close concordance with the previously reported standard values, as summarized in Table 4.1.

Table 4.1. Numerical values of the skin-friction coefficient $f''(0)$ corresponding to different magnitudes of the velocity parameter $\frac{a}{c}$, evaluated under the conditions $A = k_1 = \lambda{=}\delta = 0$.

$\frac{a}{c}$	Mahapatra and Gupta (2002)	Nazar *et al.* (2004)	Bhattacharyya *et al.* (2011)	Present study
0.1	-0.9694	-0.9694	-0.9694	-0.9694
0.2	-0.9181	-0.9181	-0.9181	-0.9181
0.5	-0.6673	-0.6673	-0.6673	-0.6673
2.0	2.0175	2.0175	2.0175	2.0175
3.0	4.7293	4.7296	4.7293	4.7292

Fig. 4.1 illustrates the non-dimensionless stream-wise velocity profiles $f'(\eta)$ parameterized by the similarity variable η, resolved across distinct magnitudes of the velocity ratio $\frac{a}{c}$, subject respectively to (a) velocity–slip and (b) no–slip boundary impositions. For the regime $\frac{a}{c} > 1$, the momentum boundary-layer thickness exhibits a monotonic reduction with increasing $\frac{a}{c}$, while for $\frac{a}{c} < 1$, a similar diminishing trend with respect to $\frac{a}{c}$, is observed. Conversely, at the critical condition $\frac{a}{c} = 1$, the boundary-layer structure ceases to exist, thereby reflecting the intrinsic fluid dynamic behaviour at the stagnation configuration. Moreover, it is observed that slip at the wall augments momentum-diffusive layer thickness, whereas under no-slip conditions, a comparatively thinner boundary layer is sustained.

Figs. 4.2 and 4.3 present the velocity distributions $f'(\eta)$ versus the similarity coordinate η for varying porosity parameter k_1 under (a) velocity-slip and (b) no-slip boundary constraints, corresponding to $\frac{a}{c} = 1.5$ & $\frac{a}{c} = 0.5$, respectively. The trends in Fig. 4.3 reveal that the velocity field initially increases; however, with further augmentation of k_1 , a progressive retardation in the fluid motion is observed within slip-enabled and slip-suppressed boundary regimes. Conversely, the behaviour illustrated in Fig. 4.4 exhibits the opposite tendency, emphasizing that the velocity parameter $\frac{a}{c}$ exerts a critical influence on the acceleration and deceleration intrinsic attributes governing the spatial and temporal evolution of the fluid domain. Furthermore, the momentum boundary-layer thickness is found to intensify under slip conditions, whereas a comparatively attenuated boundary layer is sustained in the absence of slip.

Figs. 4.4 and 4.5 depict the velocity profiles $f'(\eta)$ as functions of the similarity variable η for variations in the unsteadiness parameter A under (a) velocity-slip and (b) no-slip boundary constraints, corresponding to $\frac{a}{c} = 1.5$ & $\frac{a}{c} = 0.5$. For $\frac{a}{c} = 1.5$, an increase in A initially enhances the fluid velocity at a given location; however, with further escalation of A, the velocity field attenuates, resulting in a contraction of the characteristic spatial extent over which the fluid velocity undergoes significant deviation from the free-stream, delineating the region of momentum diffusion adjacent to the solid boundary. In contrast, under both slip and no-slip boundary constraints, the boundary layer exhibits a thickening tendency with rising A, albeit accompanied by a reduction in the local velocity magnitude. A diametrically opposite trend is manifested for $\frac{a}{c} = 0.5$, signifying that the interplay between the stretching-to-straining ratio and the unsteadiness parameter fundamentally governs the momentum transport characteristics.

Fig. 4.6 portrays the velocity distributions $f'(\eta)$ with respect to the similarity coordinate η for variations in the velocity-slip parameter λ, corresponding to (a) $\frac{a}{c} = 1.5$ and (b) $\frac{a}{c} = 0.5$. For $\frac{a}{c} = 1.5$, the velocity field exhibits an increasing tendency with the augmentation of λ, whereas an entirely opposite trend is manifested for $\frac{a}{c} = 0.5$. In both regimes of $\frac{a}{c}$, however, the momentum boundary layer undergoes a rapid thinning effect as λ increases, highlighting the pronounced influence of velocity slip on near-wall shear transport.

Fig. 4.7 illustrates the temperature distributions $\theta(\eta)$ as functions of the similarity coordinate η for distinct values of the velocity parameter $\frac{a}{c}$ under (a) slip and (b) no-slip boundary conditions. An enhance in $\frac{a}{c}$ leads to a marked reduction in $\theta(\eta)$ at fixed η, thereby indicating a progressive thinning of the spatial domain over which thermal diffusion significantly alters the fluid temperature near a boundary. Furthermore, the existence of a discernible thermal boundary-layer structure is observed even at the critical condition a/c = 1.

Figs. 4.8 and 4.9 present the temperature distributions $\theta(\eta)$ with respect to the similarity coordinate η for varying porosity parameter k_1 under (a) slip and (b) no-slip boundary conditions, corresponding to $\frac{a}{c} = 1.5$ & $\frac{a}{c} = 0.5$, respectively. The trends in Fig. 4.9 indicate that the temperature initially decreases with increasing k_1, followed by a slight augmentation at higher values, whereas Fig. 4.10 reveals a diametrically opposite response. These contrasting behaviours underscore the pivotal role of the velocity ratio parameter $\frac{a}{c}$ in dictating the thermal transport characteristics of the fluid. Moreover, it is evident that the thickness of the thermal boundary layer is highly sensitive to variations in $\frac{a}{c}$, particularly under the influence of the thermal slip parameter.

Figs. 4.10 and 4.11 depict the temperature profiles $\theta(\eta)$ as functions of the similarity variable η for variations in the unsteadiness parameter A under (a) slip and (b) no-slip thermal boundary constraints. For all considered values of the velocity ratio parameter $\frac{a}{c}$, an increase in A induces a uniform reduction in the fluid temperature throughout the domain, irrespective of the imposed boundary condition. Furthermore, the thermal boundary-layer thickness exhibits an enlarging tendency as the velocity ratio parameter $\frac{a}{c}$ decreases, highlighting the strong coupling between temporal unsteadiness and stream-wise strain-to-stretching interactions in governing heat transport.

Fig. 4.12 illustrates the temperature distributions $\theta(\eta)$ with respect to the similarity coordinate η for distinct values of the velocity-slip parameter λ, corresponding to (a) $\frac{a}{c} = 1.5$ & (b) $\frac{a}{c} = 0.5$,. At a fixed location, the fluid temperature exhibits a decreasing tendency as $\frac{a}{c} = 1.5$, whereas a pronounced increase is observed when $\frac{a}{c} = 0.5$. Nevertheless, in both regimes, the

thermal boundary layer undergoes a rapid contraction with the growth of λ, underscoring the strong sensitivity of thermal transport to interfacial velocity-slip effects.

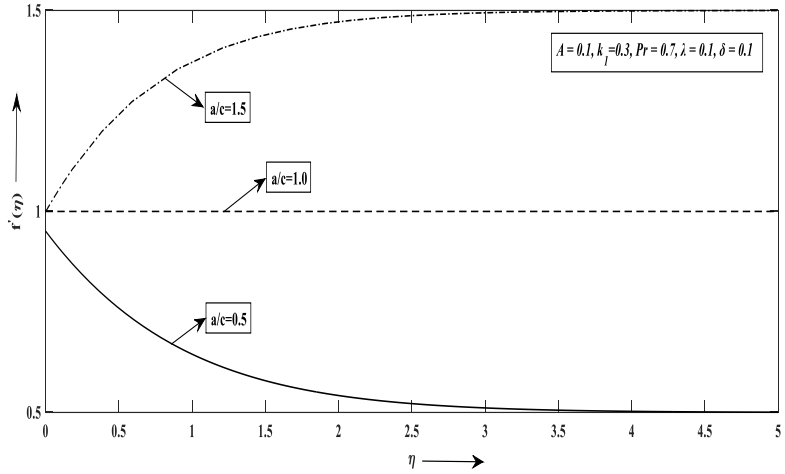

Fig.4. 2 (a) Plot of $f'(\eta)$ for variation of a/c taking $\lambda \neq 0$

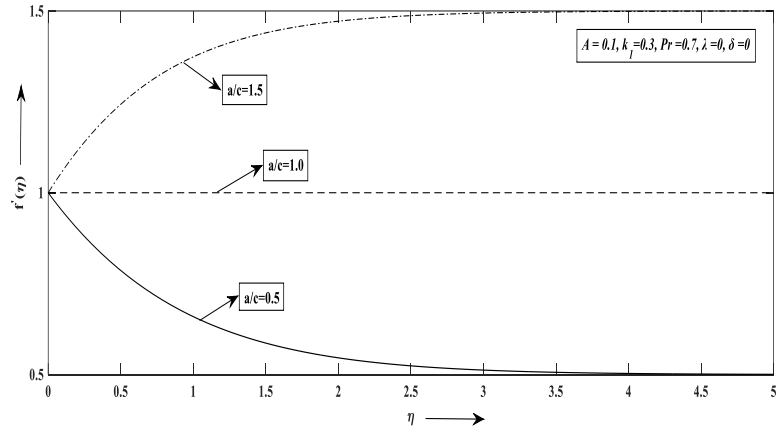

Fig.4. 2 (b) Plot of $f'(\eta)$ for variation of a/c taking $\lambda = 0$

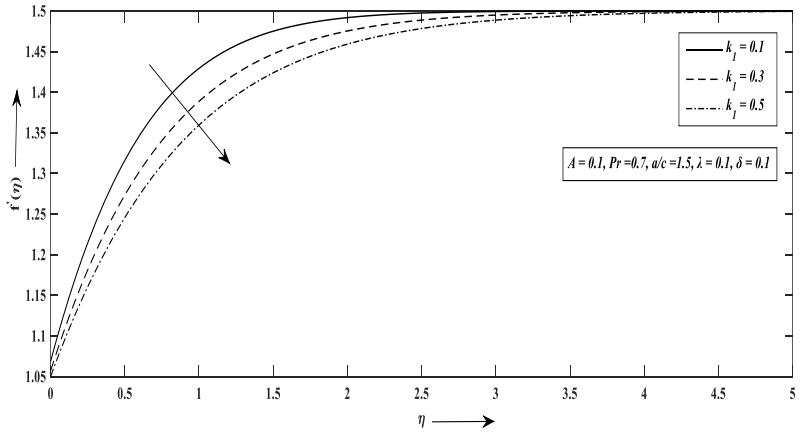

Fig. 4.3 (a) Plot of $f'(\eta)$ for variation of k_1 taking $\lambda \neq 0$ for a/c =1.5

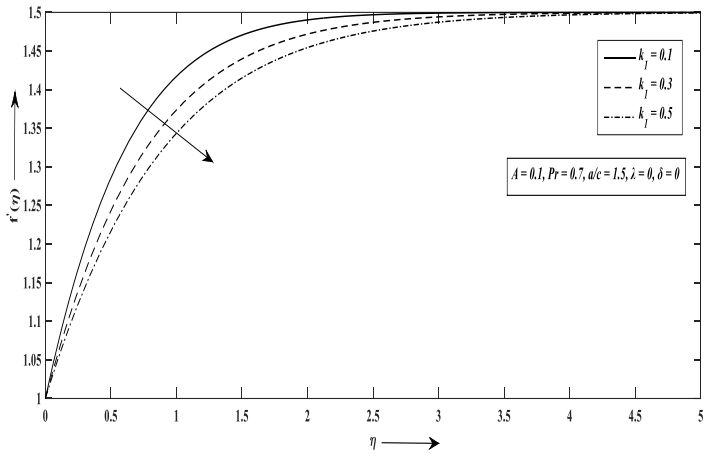

Fig. 4.3 (b) Plot of $f'(\eta)$ for variation of k_1 taking $\lambda = 0$ for a/c =1.5

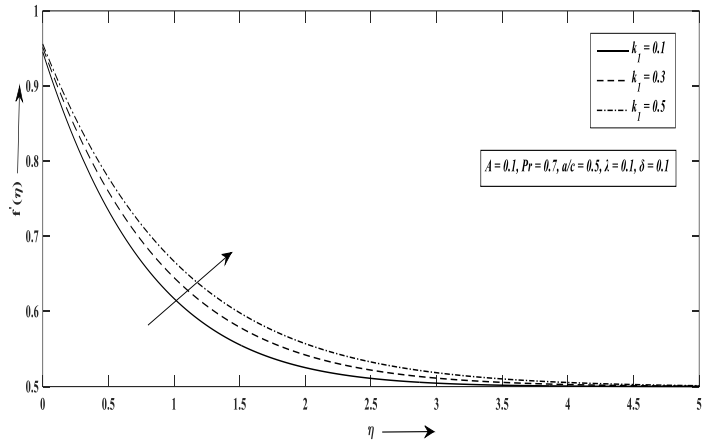

Fig. 4.4 (a) Plot of $f'(\eta)$ for variation of k_1 taking $\lambda \neq 0$ for a/c =0.5

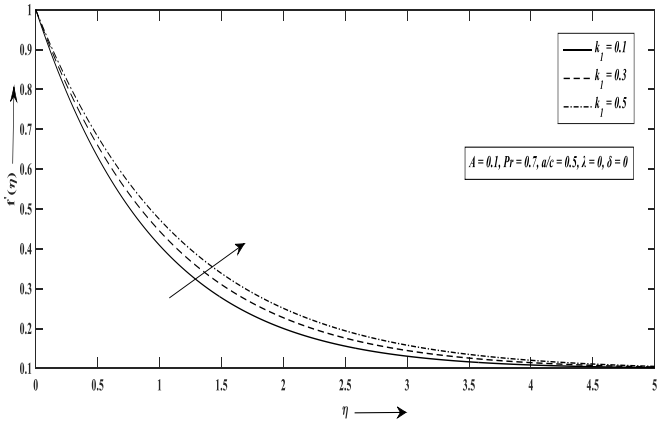

Fig. 4.4 (b) Plot of $f'(\eta)$ for variation of k_1 taking $\lambda = 0$ for a/c =0.5

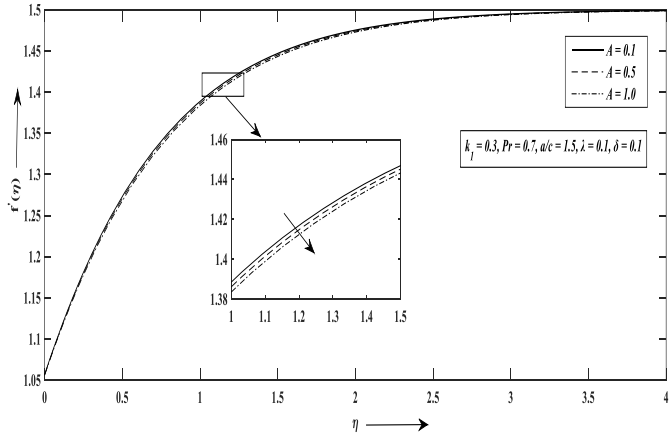

Fig. 4.5 (a) Plot of $f'(\eta)$ for variation of A taking $\lambda \neq 0$ for a/c =1.5

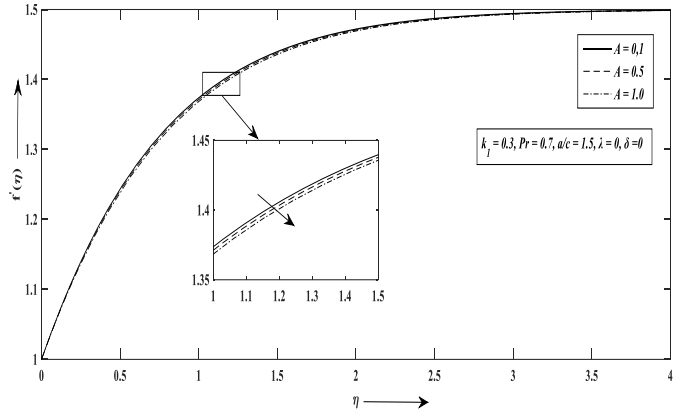

Fig. 4.5 (b) Plot of $f'(\eta)$ for variation of A taking $\lambda = 0$ for a/c =1.5

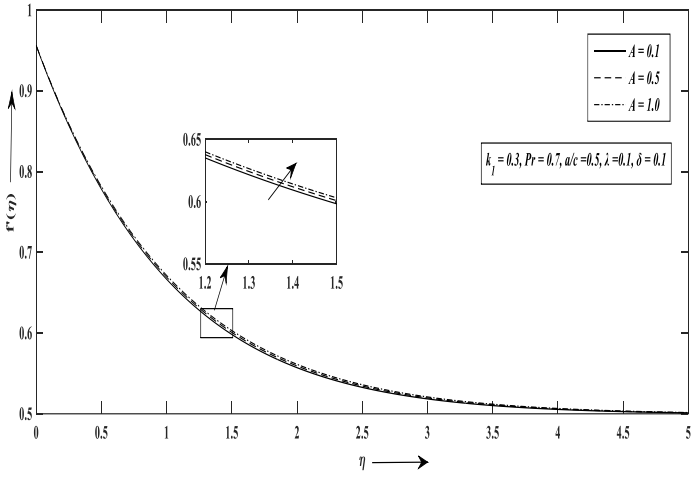

Fig. 4.6 (a) Plot of $f'(\eta)$ for variation of A taking $\lambda \neq 0$ for a/c =0.5

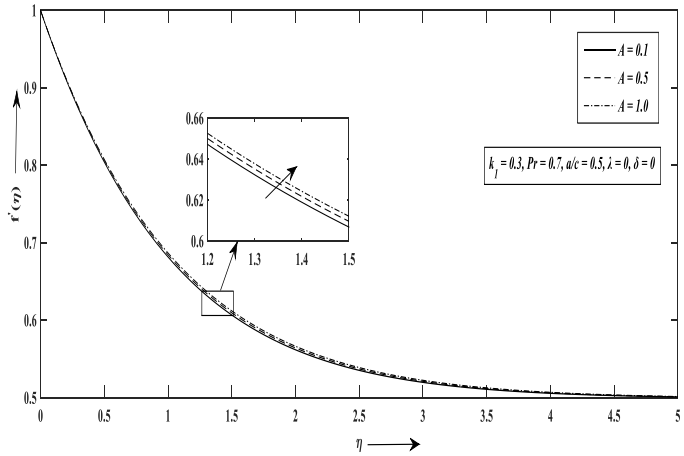

Fig. 4.6 (b) Plot of $f'(\eta)$ for variation of A taking $\lambda = 0$ for a/c =0.5

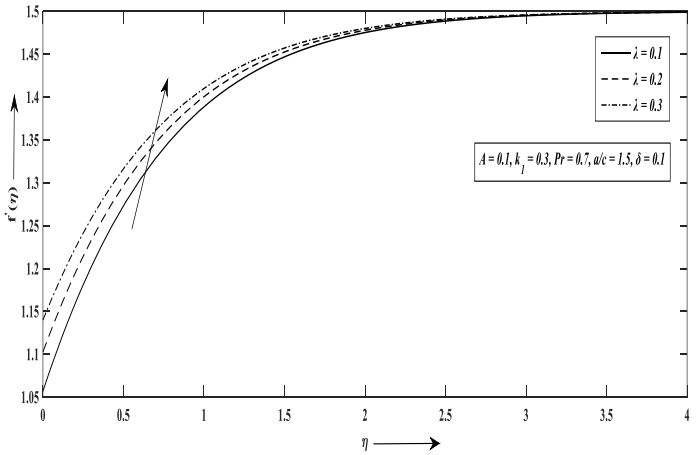

Fig. 4.7 (a) Plot of $f'(\eta)$ for variation of λ for a/c =1.5

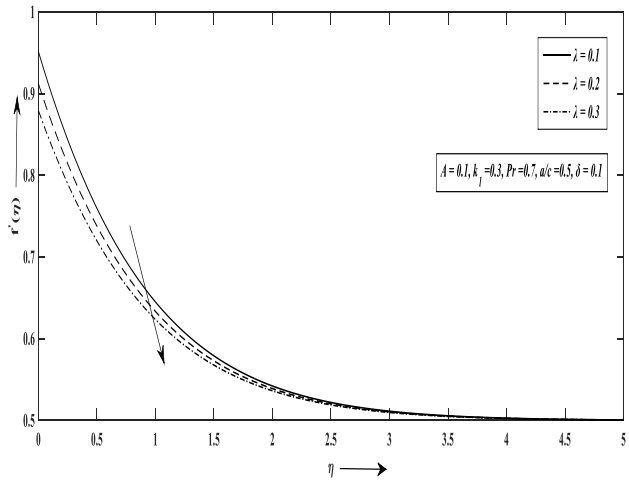

Fig. 4.7 (b) Plot of $f'(\eta)$ for variation of λ for a/c =0.5

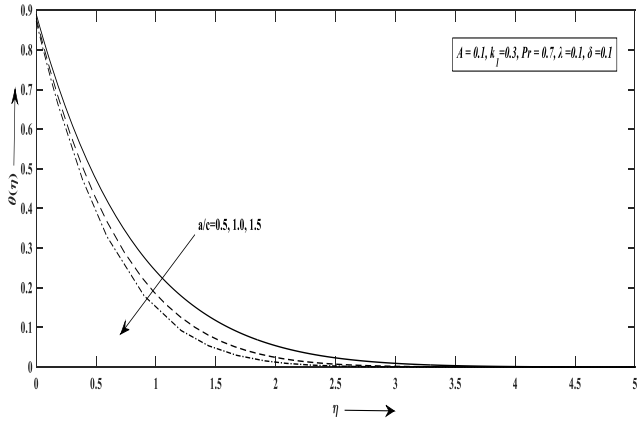

Fig.4.8 (a) Plot of $\theta(\eta)$ for variation of a/c taking $\delta \neq 0$

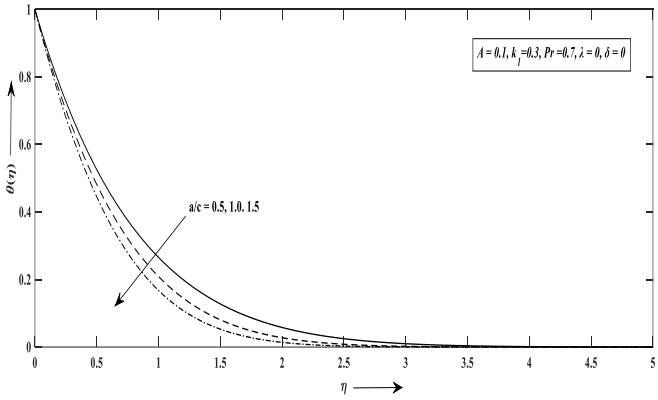

Fig.4.8 (b) Plot of $\theta(\eta)$ for variation of a/c taking $\delta = 0$

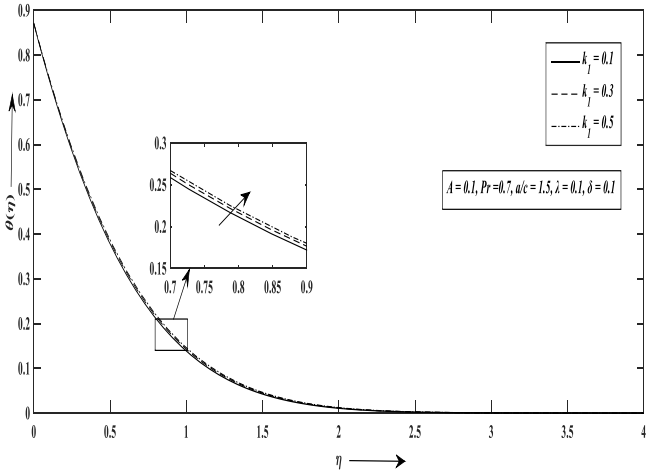

Fig.4.9 (a) Plot of $\theta(\eta)$ for variation of k_1 taking $\delta \neq 0$ for a/c =1.5

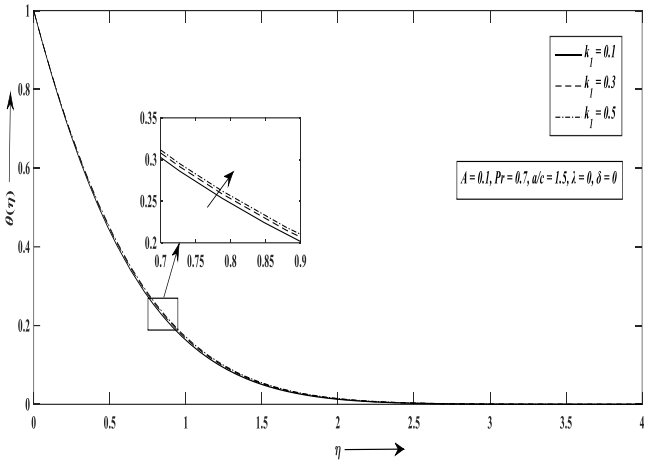

Fig.4.9 (b) Plot of $\theta(\eta)$ for variation of k_1 taking $\delta = 0$ for a/c =1.5

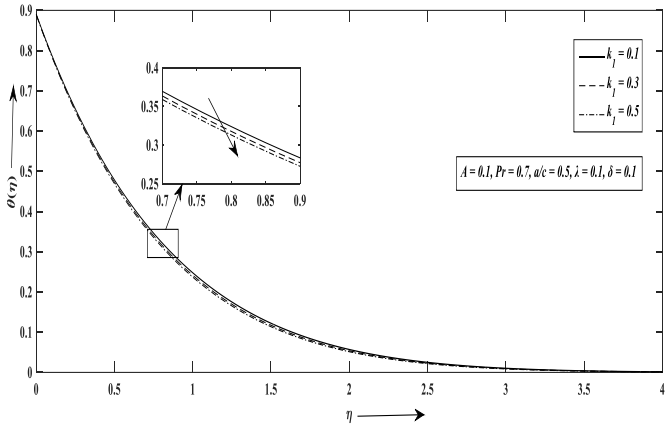

Fig. 4.10 (a) Plot of $\theta(\eta)$ for variation of k_1 taking $\delta = 0$ for a/c =0.5

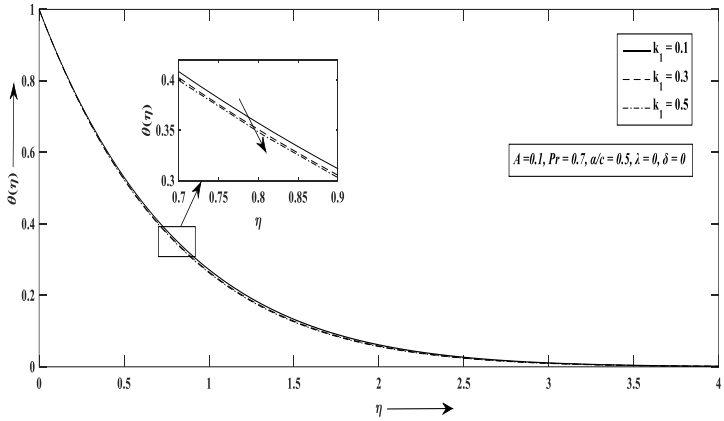

Fig. 4.10 (b) Plot of $\theta(\eta)$ for variation of k_1 taking $\delta \neq 0$ for a/c =0.5

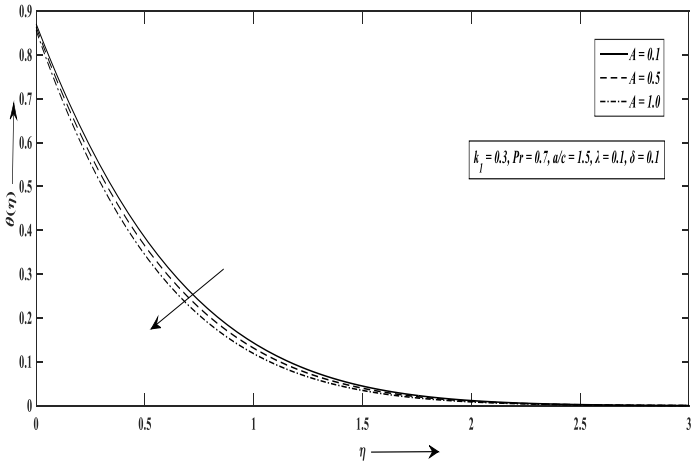

Fig.4.11(a) Plot of $\theta(\eta)$ for variation of A taking $\delta \neq 0$ for a/c =1.5

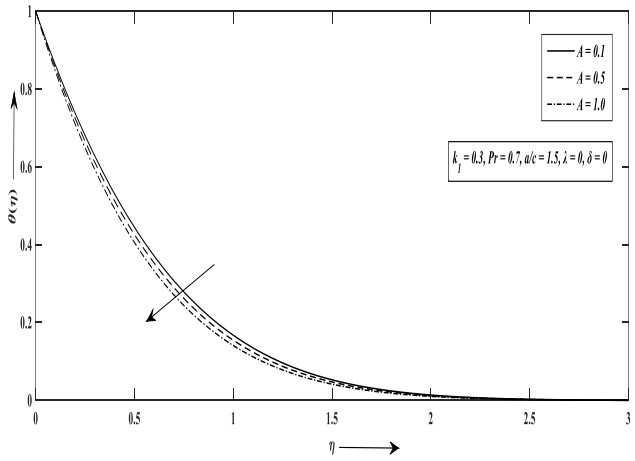

Fig.4.11(b) Plot of $\theta(\eta)$ for variation of A taking $\delta = 0$ for a/c =1.5

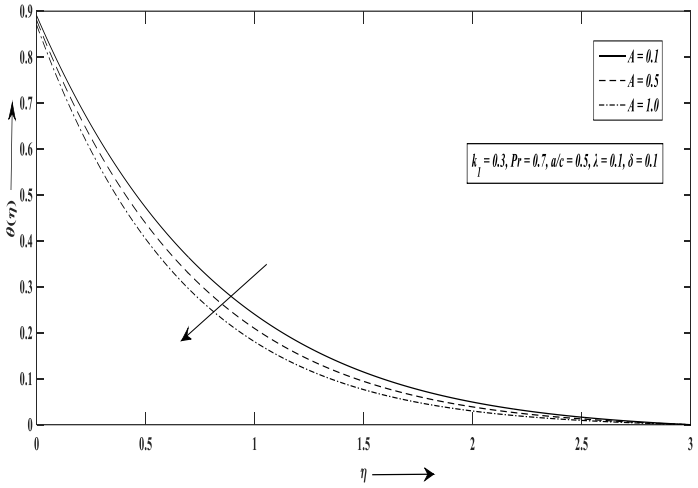

Fig. 4.12 (a) Plot of $\theta(\eta)$ for variation of A taking $\delta \neq 0$ for a/c =0.5

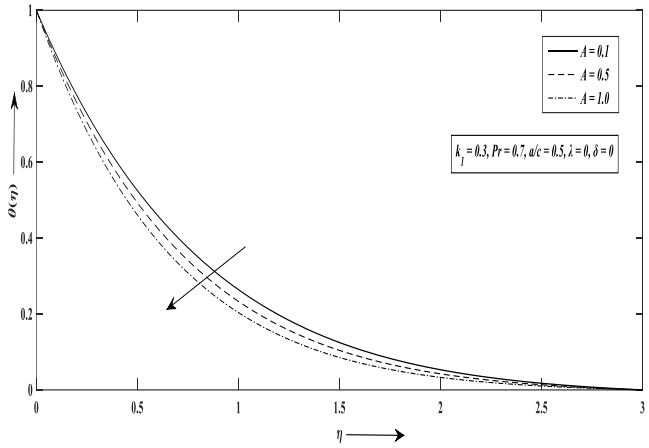

Fig. 4.12 (b) Plot of $\theta(\eta)$ for variation of A taking $\delta = 0$ for a/c =0.5

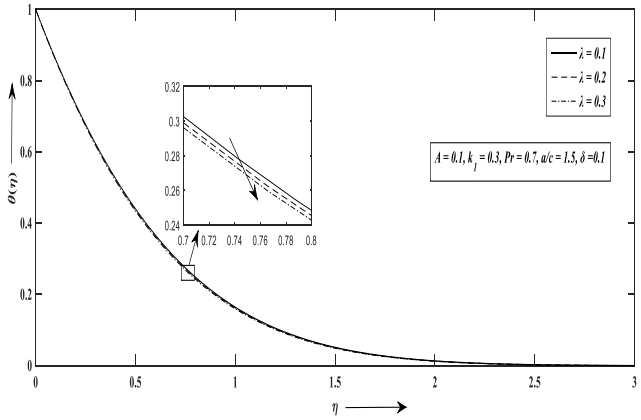

Fig. 4.13 (a) Plot of $\theta(\eta)$ for variation of λ for a/c =1.5

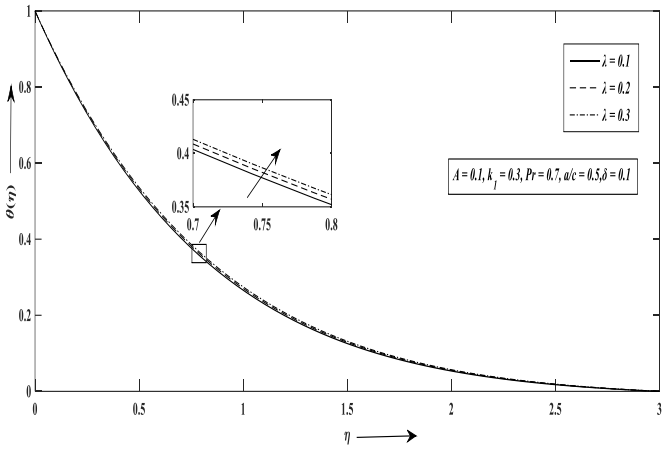

Fig. 4.13 (b) Plot of $\theta(\eta)$ for variation of λ for a/c =0.5

Conclusions

The principal inferences deduced from the present investigation can be articulated as follows:

- The rheological character of the elastico-viscous medium, in conjunction with the velocity ratio parameter, exerts a pronounced influence on the kinematic field, either amplifying or attenuating the fluid velocity depending on parametric regimes.
- The hydrodynamic and thermal transport behaviours can be effectively regulated through the appropriate tuning of the dimensionless parameters characterizing tangential momentum and thermal discontinuities at the boundary interface.
- The magnitude of thermal energy transport exhibits a consistent attenuation with the progressive increase in nearly all governing flow parameters.
- The unsteadiness parameter exerts a critical influence in augmenting the rate of thermal transport throughout the fluid region.
- The velocity ratio parameter manifests a dominant impact on the overall fluid dynamic characteristics.
- The slip coefficients serve as effective regulators of the characteristic extent of the region over which momentum diffusion occurs adjacent to a surface under both slip and no-slip configurations.
- Control over the boundary-layer development can be systematically achieved through the modulation of slip parameters.

Acknowledgements

The author expresses profound gratitude to the anonymous reviewers for their meticulous evaluation and constructive observations, which significantly enhanced the technical rigor and clarity of the manuscript. Sincere acknowledgment is also extended to the editorial board of the journal for their valuable time and consideration. The computational experiments were carried out independently without institutional or external financial support, and hence the author gratefully recognizes the self-driven nature of this scholarly endeavor.

Conflict of Interest

The author declares no conflicts of interest and confirms that this research was conducted independently by me without external funding or sponsorship.

Authors Contribution

B.K. Saha:

The entirety of the research endeavor—including the intellectual conception of the problem, formulation of the elastico–viscous boundary-layer framework, mathematical modeling, and imposition of slip and no-slip boundary constraints—was independently executed by the sole author. The algorithmic deployment of the MATLAB *bvp4c* solver for the nonlinear boundary-value problem, numerical validation, and diagnostic exploration of the hydrodynamic and thermal field behaviors were accomplished exclusively by the author. Comprehensive analysis of parameter sensitivities, physical interpretations of the velocity and temperature distributions, as well as the critical evaluation of momentum and thermal boundary-layer thicknesses,

were likewise carried out by the author. Manuscript composition, technical refinement, integration of relevant literature, and final preparation for submission were undertaken in their entirety by the same. The research thus represents an autonomous scholarly effort with no collaborative or external involvement.

REFERENCES

[1]. Mahapatra, T. R., & Gupta, A. S. (2002). Heat transfer in stagnation-point flow towards a stretching sheet. *Heat and Mass Transfer, 38*(6), 517–521. https://doi.org/10.1007/s002310100215

[2]. Nazar, R., Norsarahaida, A., & Pop, I. (2004). Unsteady boundary layer flow in the region of the stagnation point on a stretching sheet. *International Journal of Engineering Science, 42*(11–12), 1241–1253. https://doi.org/10.1016/j.ijengsci.2003.12.002

[3]. Hayat, T., Javed, T., & Abbas, Z. (2009). MHD flow of a micropolar fluid near a stagnation-point towards a non-linear stretching surface. *Nonlinear Analysis: Real World Applications, 10*(3), 1514–1526. https://doi.org/10.1016/j.nonrwa.2008.01.019

[4]. Mukhopadhyay, S. (2010). Effects of slip on unsteady mixed convective flow and heat transfer past a stretching surface. *Chinese Physics Letters, 27*(12), 124401. https://doi.org/10.1088/0256-307X/27/12/124401

[5]. Ishak, A., Nazar, R., & Pop, I. (2008). Heat transfer over an unsteady stretching surface with prescribed heat flux. *Canadian Journal of Physics, 86*(6), 853–855. https://doi.org/10.1139/p08-005

[6]. Bhattacharyya, K., Mukhopadhyay, S., & Layek, G. C. (2011). Slip effects on boundary layer stagnation-point flow and heat transfer towards a shrinking sheet. *International Journal of Heat and Mass Transfer, 54*(1–3), 308–313. https://doi.org/10.1016/j.ijheatmasstransfer.2010.09.041

[7]. Bhattacharyya, K. (2013). Boundary layer stagnation-point flow of Casson fluid and heat transfer towards a shrinking/stretching sheet. *Frontiers in Heat and Mass Transfer, 4*(2), 023003. https://doi.org/10.5098/hmt.v4.2.3003

[8]. Aurangzaib, M. K., Bhattacharyya, K., & Shafie, S. (2016). Multiple solutions of an unsteady stagnation-point flow with melting heat transfer in a Darcy–Brinkman porous medium. *Nonlinear Engineering, 5*(2), 99–106. https://doi.org/10.1515/nleng-2015-0034

[9]. Seth, G. S., Singha, A. K., Mandal, M. S., Maiti, D. *et al.* (2017). MHD stagnation-point flow and heat transfer past a non-isothermal shrinking/stretching sheet in porous medium with heat sink or source effect. *International Journal of Mechanical Sciences, 134,* 98–111. https://doi.org/10.1016/j.ijmecsci.2017.09.049

[10]. Dzulkifli, N. F., Bachok, N., Yacob, N. A., Arifin, N. M., Pop, I. *et al.* (2018). Unsteady stagnation-point flow and heat transfer over a permeable exponential stretching/shrinking sheet in nanofluid with slip velocity effect: A stability analysis. *Applied Sciences, 8*(11), 2172. https://doi.org/10.3390/app8112172

[11]. Rosali, H., Badlishah, M. N., Johari, M. A. M., Arifin, N. M., Pop, I., *et al.* (2020). Unsteady boundary layer stagnation-point flow and heat transfer over a stretching sheet in a porous medium with slip effects. *CFD Letters, 12*(10), 52–61. https://doi.org/10.37934/cfdl.12.10.5261

[12]. Layek, G. C., Mandal, B., Bhattacharyya, K., Uddin, M. J., *et al.* (2018). Lie symmetry analysis of boundary layer stagnation-point flow and heat transfer of non-Newtonian power-law fluids over a nonlinearly shrinking/stretching

sheet with thermal radiation. *International Journal of Nonlinear Sciences and Numerical Simulation, 19*(3–4), 415–426. https://doi.org/10.1515/ijnsns-2017-0211

[13]. Fazle, M., & Stanford, S. (2019). Multiple slip effects on MHD unsteady flow heat and mass transfer impinging on permeable stretching sheet with radiation. *Modelling and Simulation in Engineering, 2019,* Article 3052790, 1–11. https://doi.org/10.1155/2019/3052790

[14]. Alghamdi, W., Gul, T., Nullah, M., Khan, I., Tlili, I., *et al.* (2021). Boundary layer stagnation-point flow of the Casson hybrid nanofluid over an unsteady stretching surface. *AIP Advances, 11*(1), 015130. https://doi.org/10.1063/5.0036232

[15]. Agrawal, R., & Kaswan, P. (2021). Effect of slip condition on MHD flow and heat transfer through a permeable nonlinearly stretching sheet in a porous medium using the homotopy analysis method. *Computational Thermal Sciences: An International Journal, 13*(1), 1–15. https://doi.org/10.1615/ComputThermalScien.2020033258

[16]. Mabood, F., Abbasi, A., Farooq, W., Khan, U., & Chu, Y.-M., *et al.* (2022). Effects of non-linear radiation and chemical reaction on Oldroyd-B nanofluid near oblique stagnation-point flow. *Chinese Journal of Physics, 77,* 1197–1208. https://doi.org/10.1016/j.cjph.2022.03.049

[17]. Debnath, K., & Saha, B. K. (2020). Solution of non-Newtonian boundary layer flow in a convergent channel using homotopy perturbation method. *Transient, A Journal of Natural Sciences and Allied Subjects, 8,* 28–32

[18]. Debnath, K., & Saha, B. K. (2020). Hydromagnetic visco-elastic boundary layer flow past an exponentially stretching sheet with suction or blowing. In A. K. Sharma, R. S. Rajesh, & A. Thakur (Eds.), *Emerging technologies in data mining and information security: Proceedings of IEMIS 2020* (Vol. 1, pp. 533–541). Springer. https://doi.org/10.1007/978-981-15-9927-9

[19]. Debnath, K., & Saha, B. K. (2022). Heat and partial slip impact on elastico-viscous fluid flow past a flat permeable plate. *Mathematical Forum, 29,* 66–78.

[20]. Debnath, K., & Saha, B. K. (2022). Slip flow and heat transition for hydromagnetic elastico-viscous fluid past a flat moving plate. *Emerging technologies in data mining and information security: Proceedings of IEMIS 2022* (Vol. 1, pp. 131–140). Springer. https://doi.org/10.1007/978-981-19-4193-1

[21]. https://doi.org/10.1007/978-981-19-4193-1

[22]. Saha, B. K., & Debnath, K. (2023). Reactive solute diffusion in elastico-viscous fluid past a flat permeable plate. *High Technology Letters, 29*(7), 303–310.

[23]. Raza, J., & Ashfaq, A. (2025). Optimization of heat transfer in two-phased nanofluid flow over a biaxial sheet using Taguchi-GRA method. *Multiscale and Multidisciplinary Modeling, Experiments and Design, 8,* 124. https://doi.org/10.1007/s41939-024-00712-z

[24]. Raza, J., & Mustafa, F., Shah, Z., *et al.* (2024). Optimization of heat transfer rate of trihybrid nanofluid embedded between two horizontal coaxial cylinders by RSM. *Case Studies in Thermal Engineering, 46,* 104637. https://doi.org/10.1016/j.csite.2024.104637

[25]. Raza, J., Baloch, L. A. L., *et al.* (2024). Fuzzy TOPSIS optimization of MHD trihybrid nanofluid in heat pipes. *Case Studies in Thermal Engineering, 49,* 105493. https://doi.org/10.1016/j.csite.2024.105493

[26]. Shutaywi, M., Raza, J., *et al.* (2024). Optimization of heat transfer in a channel with stretching walls using a magnetized tetra-hybrid nanofluid. *Advances in Mechanical Engineering, 16*(11), 1–19. https://doi.org/10.1177/16878132241293959

[27]. Shutaywi, M., Raza, J., *et al.* (2025). Integrated Taguchi-GRA-PCA for optimizing the heat transfer performance of trihybrid Casson nanofluid flow over a stretching sheet with quadratic velocity. *Journal of Radiation Research and Applied Sciences, 18,* 101570. https://doi.org/10.1016/j.jrras.2025.101570

[28]. Bhattacharyya, K., Mukhopadhyay, S., & Layek, G. C. (2011). Slip effects on an unsteady boundary layer stagnation-point flow and heat transfer towards a stretching sheet. *Chinese Physics Letters, 28*(9), 094702. https://doi.org/10.1088/0256-307X/28/9/094702

NOMENCLATURE

$(u_x, v_y, \mathrm{u_t})$	Components of fluid velocities (m/s)
p_x	Pressure in x-direction (N/m^2)
(T_t, T_x, T_y, T_{yy})	Components of fluid ($N.s/m^2$)
T_∞	Free Stream Temperatures (K)
T_0	Constant surface temperature (K)
k_0	Elastico- Viscous Parameter ($Kg.m^{-1}.s^{-1}$)
k_1	Non-Newtonian Parameter ($Kg.m^{-1}.s^{-1}$)
$\frac{a}{c}$	Velocity Ratio Parameter
A	Unsteadiness Parameter
c_p	Specific Heat (J/Kg.K)
u_∞(x,t)	Stagnation Flow Velocity (m/s)
u_w(x,t)	Stretching Velocity (m/s)
c	Stretching Parameter
a	Straining Parameter (m/m)
N_1	Velocity Slip Coefficient
N	Initial Velocity Slip Coefficient
D_1	Thermal Slip Coefficient
D	Initial Thermal Slip Coefficient
p_r	Prandtl Number

GREEK LETTERS

ρ	Fluid density (Kg/m^3)
υ	Kinematic Viscosity (m^2/s)
K	Thermal Conductivity (W/m.K)
Ψ	Stream Function (m^2/s)
θ	Temperature Function (K)
η	Similarity Variable
λ	Transformed Velocity Slip Parameter
δ	Transformed Thermal Slip
α	Constant

Cite this Article:

Saha, B. K. (2026). Transient Elastico-Viscous Boundary Layer Thermal Transport with Stagnation-Point Slip Flow Over a Stretching Surface. Pi International Journal of Mathematical Sciences, 2(2), 16–31.

Journal URL: *https://pijms.com/*

DOI: *https://doi.org/10.59828/pijms.v2i2.30*